

**Title: Flexible BiSeI/NiO-based X-ray synapses bridging the functions of detection and memory**

**Authors:** Qiao Wang,<sup>1,2</sup> Pengfei Li,<sup>3</sup> Yushou Song,<sup>3</sup> Jalu Li,<sup>1,4</sup> Haiying Xiao,<sup>1,4</sup> Yuqing Wang,<sup>1,4</sup> Guoliang Ma,<sup>5</sup> Hsu-Sheng Tsai,<sup>6\*</sup> Ping-An Hu<sup>1,4\*</sup>

**Affiliations:**

<sup>1</sup>Key Laboratory of Micro-Systems and Micro-Structures Manufacturing, Harbin Institute of Technology, 150001, Harbin, China.

<sup>2</sup>School of Chemistry and Chemical Engineering, Harbin Institute of Technology, 150001, Harbin, China.

<sup>3</sup>College of Nuclear Science and Technology, Harbin Engineering University, 150001, Harbin, China.

<sup>4</sup>School of Materials Science and Engineering, Harbin Institute of Technology, 150001, Harbin, China.

<sup>5</sup>Laboratory for Space Environment and Physical Sciences, Harbin Institute of Technology, 150001, Harbin, China.

<sup>6</sup>School of Physics, Harbin Institute of Technology, 150001, Harbin, China.

\*Corresponding author. Email: [hstsai@hit.edu.cn](mailto:hstsai@hit.edu.cn) (H.S.T.), [hupa@hit.edu.cn](mailto:hupa@hit.edu.cn) (P.A.H.)

**Abstract:**

Currently, the X-ray detectors are widely used in medical imaging, industrial inspection, aerospace, and other fields, as the market demand for high-efficiency, flexible, and low-power detectors is increased. Although the traditional inorganic X-ray detection materials have achieved great success and effectiveness, they have their own limitations and let alone flexibility/bendability and memory function. In this study, we present the design of a BiSeI/NiO-V<sub>Ni</sub>-based X-ray synaptic detector and its application in the simulation of biological synaptic processes. Herein, the BiSeI, a quasi-1D inorganic semiconductor, stands out as an ideal choice for the X-ray detectors, especially for flexible and portable devices due to its large atomic number, large photoelectric absorption coefficient, and mechanical plasticity. Meanwhile, the NiO-based materials provide the memory function required for the intelligent detection systems. Moreover, our devices offer notable advantages in terms of low power consumption, compared with traditional X-ray detectors. The BiSeI/NiO-V<sub>Ni</sub> detectors demonstrate advanced features with an ultrahigh sensitivity of  $1.35 \times 10^6 \mu\text{C Gy}_{\text{air}}^{-1} \text{cm}^{-2}$ , an ultralow detection limit of  $34 \text{ nGy s}^{-1}$ , and include the paired-pulse facilitation (PPF) and the transition from short- to long-term memory, maintaining the functionality on flexible substrates. This design represents a significant step toward the development of intelligent and flexible X-ray detectors.

## Main text:

### Introduction

With the advancement of artificial intelligence (AI) technology, the development of intelligent radiation detectors<sup>1-3</sup> integrating the detection, storage, and computation has become an inevitable trend. The data processing of traditional radiation detectors is largely based on the von Neumann architecture, where the central processing unit (CPU) retrieves data from memory and processes it sequentially. However, this architecture encounters significant challenges such as complex data processing, transmission bottlenecks, and high energy consumption as the volume of data (e.g. frame rate, pixels, and bits) is increased with the advancement of imaging technology. These issues are particularly problematic in the applications requiring rapid data processing<sup>4</sup>, such as the real-time medical imaging for surgery, robotic surgery, and telesurgery, where the delays in data processing or signal latency can adversely affect the therapy for patients.

Currently, the traditional materials for radiation detection, such as CsI, amorphous selenium (a-Se), CdTe, and CdZnTe, are lack of inherent storage and computing capabilities. Not only that, they have other drawbacks, such as low atomic number ( $Z$  value), poor carrier transport, toxicity, and instability. The commercial X-ray imagers predominantly utilize a-Se as the functional material. However, its relatively low  $Z$  value (34) as well as limited product of carrier mobility and lifetime ( $\mu\tau \sim 10^{-7} \text{ cm}^2 \text{ V}^{-1}$ ) restrict its ability to detect the X-rays with low dose rates. Although the CsI:Tl possesses a higher  $Z$  value, the detection accuracy and spatial resolution would be reduced as it is operated as an indirect X-ray detector through scintillation. Furthermore, the CsI, an ionic salt, is highly hygroscopic and the presence of toxic Tl dopant raises the concerns about safety and environmental risks during its production, use, and disposal. Despite recent progress<sup>5-7</sup> in the perovskite-based materials for radiation detection, the ion migration in halide perovskites is prone to occur<sup>8-12</sup> under high electric fields and/or high-energy radiation, leading to material degradation and device failure. These limitations hinder the broader application of perovskites for the radiation detection technologies. Moreover, conventional inorganic X-ray detection materials are generally brittle, making it inexpedient for design, fabrication, and integration in applications requiring the special surface or angular configurations (e.g.  $4\pi$  angle radiation measurement<sup>13-15</sup>, PET/CT<sup>16</sup>) and the wearable/portable devices (e.g. nuclear detection robots<sup>17-19</sup>, space exploration spectrometers<sup>20</sup>, Rn contamination monitors<sup>21</sup>).

To address these challenges, it is critical to simplify the conventional X-ray detection system. One promising approach is the use of retinal photosynaptic detectors<sup>22-25</sup> inspired by bionic principles. Neuromorphic computing architectures, which emulate the information processing functions of biological synapses and nervous systems, enable the X-ray detectors to become more efficient, intelligent, lightweight, and energy-efficient. We have demonstrated the BiSeI/NiO- $V_{\text{Ni}}$  ( $V_{\text{Ni}}$ : nickel vacancies) heterojunctions with significant potential for the retinal photosynaptic X-ray detection. The BiSeI single crystal not only satisfies the requirements of high  $Z$  value ( $Z = 83$ ),

stability, and non-toxicity, but also exhibits remarkable mechanical plasticity. On the other hand, the NiO- $V_{Ni}$  polycrystalline film with abundant nickel vacancies serves as the memory component in the detector. To the best of our knowledge, the X-ray detectors with memory functionality on the flexible substrates have not been reported.

Designing a radiation detector with memory function is already a formidable challenge, let alone designing the radiation detection material with mechanical plasticity.<sup>3,26</sup> Typically, the Bi-based materials, such as bismuth chalcogenides, bismuth halides, and others (e.g. BiOI, BiVO<sub>4</sub>, Cs<sub>3</sub>Bi<sub>2</sub>I<sub>9</sub>), are brittle.<sup>27</sup> While there have been reports on the mechanical plasticity of Bi-based materials like Mg<sub>3</sub>Bi<sub>2</sub><sup>28,29</sup> and Bi<sub>2</sub>Te<sub>3</sub><sup>30</sup>. The Mg<sub>3</sub>Bi<sub>2</sub><sup>31,32</sup> is a semimetal rather than a semiconductor and the Bi<sub>2</sub>Te<sub>3</sub> is an inherent brittle material that requires additional defects to achieve mechanical plasticity. It is even more regrettable that the bandgap of Bi<sub>2</sub>Te<sub>3</sub> is too narrow to be detect the radiation. In fact, the high-density defects usually cause a decline of  $\mu\tau$  product in semiconductors, which is not conducive to the radiation detection.<sup>33-35</sup> However, the defects can realize the memory function, so that we have to balance the memory and detection performances. To date, BiSeI is the only intrinsically plastic Bi-based semiconductor with significant potential for the X-ray detection. It is also the plastic inorganic semiconductor with the highest  $Z$  value. The BiSeI has a theoretical bandgap of 1.57 eV<sup>36</sup>, which lies within the ideal range for radiation detection. Additionally, its  $\mu\tau$  product reaches  $1.7 \times 10^{-4} \text{ cm}^2 \text{ V}^{-1}$ , which is three orders of magnitude greater than that of commercial X-ray detection materials such as a-Se<sup>33</sup>. The intelligent X-ray detector developed using the BiSeI/NiO- $V_{Ni}$  demonstrates advanced capabilities, including paired-pulse facilitation (PPF), transition from short-term to long-term memory (STM/LTM), performance stability on a flexible substrate, as well as learning and forgetting behaviors.

## Results

BiSeI, a quasi-one-dimensional (quasi-1D) chain material, is an N-type<sup>37</sup> semiconductor with an orthorhombic crystal structure, belonging to the Pnma space group. The crystal structure consists of a double chain of [(BiSeI)<sub>∞</sub>]<sub>2</sub> aligned along the b-axis as shown in Figure 1A. In this structure, the Bi and Se atoms are covalently bonded each other, while the iodine (I) atoms ionically bond with the covalent structures of BiSe. The interaction between the double chains is primarily the weak van der Waals force. This distinctive quasi-1D structure causes BiSeI to typically grow in one direction, forming a wire- or rod-shaped crystal.

Single crystals of BiSeI can be synthesized using a chemical vapor transport (CVT) method, where the iodine (I<sub>2</sub>) serves as the transport agent. In this study, the modified synthesis method based on the previous report<sup>38</sup> is depicted in Figure S1. Stoichiometric amounts of Bi (5N), Se (5N), and I<sub>2</sub> (4N) were used in the ratio of  $N_{Bi} : N_{Se} : N_{I} = 1:1:1.03$ , where the 3%-excess I<sub>2</sub> can compensate for its volatilization during the synthesis. The total raw materials of 10 g were loaded into a quartz tube, which was then vacuum-sealed at 1000 Pa. The quartz tube, with dimensions of 20 cm in length and 3 cm in diameter, was baked at 300 °C for 24 hours to fully melt and

mix the raw materials. The quartz tube was subsequently placed in the middle of a horizontal tube furnace with dual heating zone, where the low-temperature zone was set at 485 °C and the high-temperature zone containing raw materials was fixed at 500 °C. The temperature gradient across an interval of 10 cm between the two zones was maintained for 15 days. After this period, the furnace was gradually cooled down to room temperature, resulting in the growth of black stick-like single crystals in the low-temperature zone. As shown in Figure 1B, the BiSeI single crystal is unusually soft and can be bent into various shapes, such as the letter "nucleus". No fractures were observed in the bending BiSeI crystal, which was confirmed by the scanning electron microscopy (SEM) images (Figure 1D and Figure S2A). To the best of our knowledge, this is the first report of a plastic inorganic semiconductor with a quasi-1D structure. Unlike the plastic 2D layered semiconductors, the plastic quasi-1D/1D inorganic ones with superior mechanical properties are underexplored.

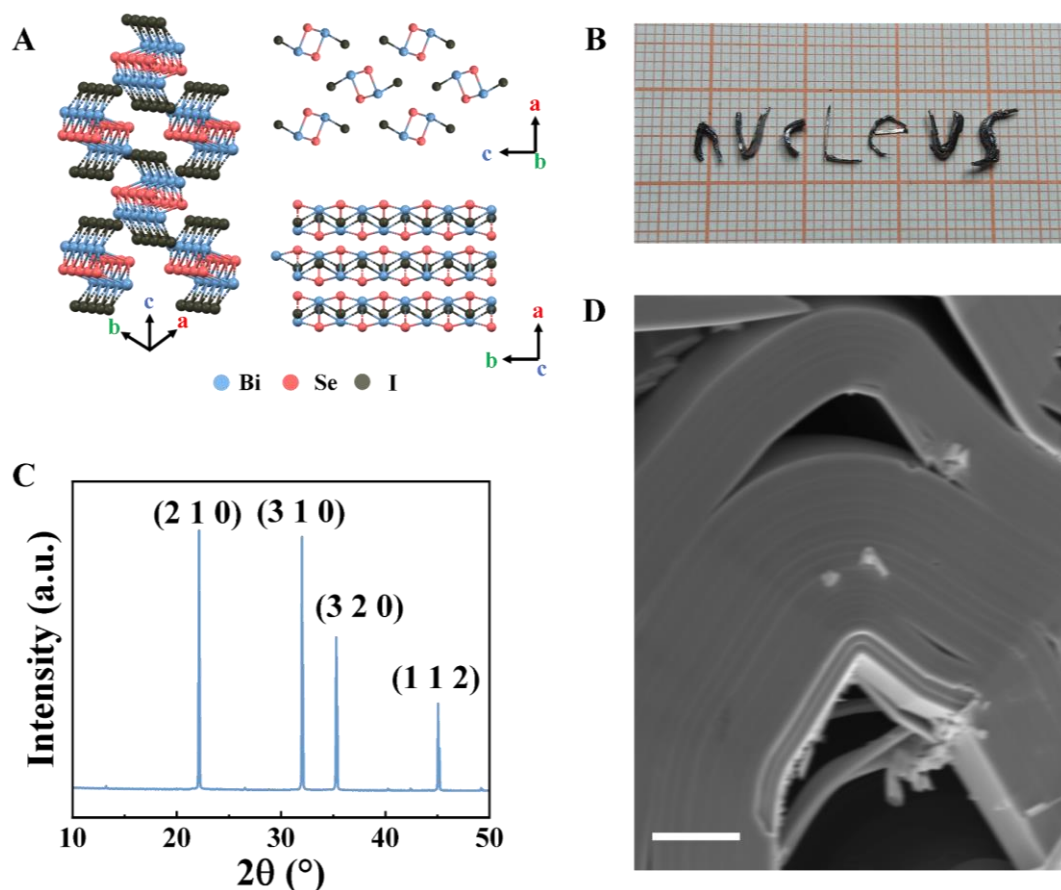
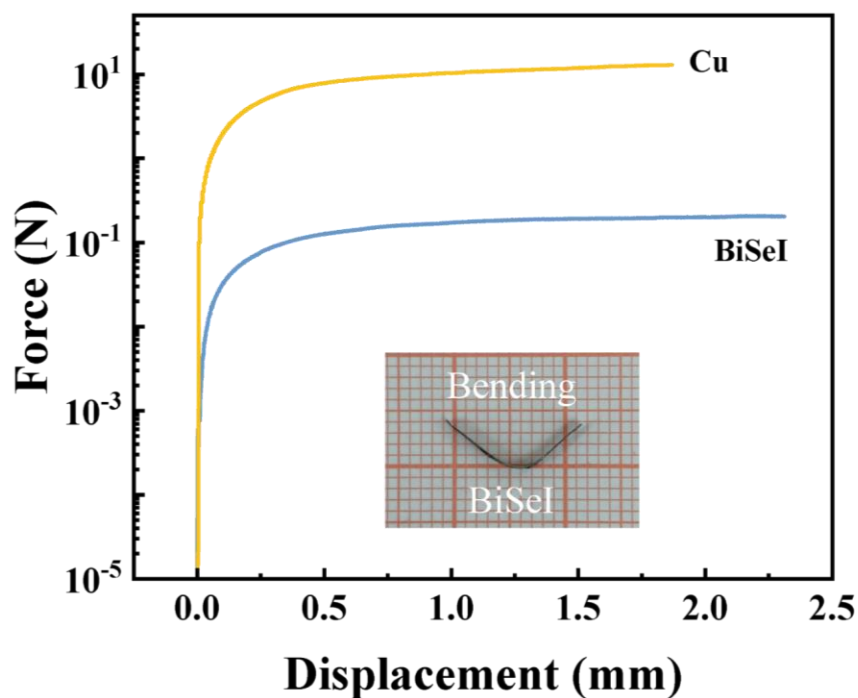


**Fig. 1.** Synthesis of BiSeI single crystal. (A) The crystal structure of BiSeI and the views along b and c axes, respectively. (B) BiSeI single crystals are bent into various letters "nucleus" without breaking. The smallest grid denotes 1 mm in the photograph. (C) XRD pattern of BiSeI single crystal. (D) SEM image of a bent BiSeI single crystal. The scale bar is 10 μm.

The energy dispersive spectroscopy (EDS) analysis (Figure S2B) clearly shows the characteristic peaks of Bi, Se, and I, with an atomic ratio of approximately 1:1:1. The EDS mapping (Figures S2C-E) confirms that the three elements are evenly distributed

throughout the crystal, indicating the high-quality synthesized material without phase separation. The X-ray diffraction (XRD) pattern shown in Figure 1C reveals sharp diffraction peaks at  $22.1^\circ$ ,  $32.0^\circ$ ,  $35.3^\circ$ , and  $45.1^\circ$ , corresponding to the (210), (310), (320), and (112) crystal planes of BiSeI, respectively. The narrow width of these XRD peaks further indicates high crystallinity. The Raman spectrum (Figure S3) also exhibits the characteristic peaks of BiSeI single crystal, confirming the successful synthesis of BiSeI again.

**A**



**B**

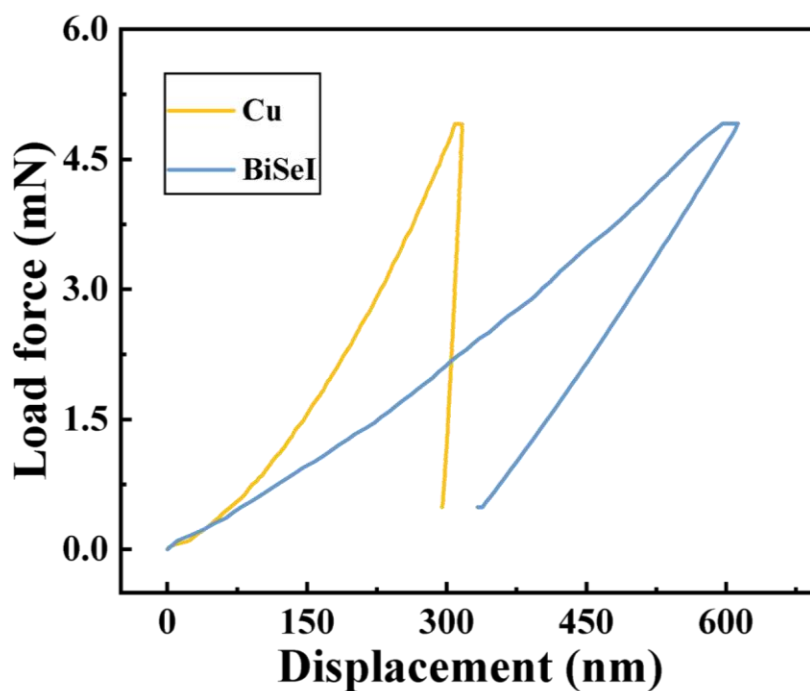


**Fig. 2.** Mechanical properties of BiSeI single crystal. (A) Force-displacement curves for bending test performed on the BiSeI and polycrystalline copper (Cu) at room temperature. The inset is an optical image of deformed BiSeI single crystal after three point bending test. (B) Nanoindentation tests with the maximum load force of 5mN for BiSeI and Cu.

The BiSeI single crystal exhibits excellent mechanical properties as it is subjected to stress. To vividly demonstrate its mechanical plasticity, a three-point bending test with a span of 10 mm as shown in Figure 2A was performed on a BiSeI single crystal sample with the dimensions of 15×3×0.25 mm<sup>3</sup>. According to the bending stress formula (ASTM Standard Test Method: D 790):

$$\delta_f = \frac{3PL}{2bd^2} \quad (1)$$

where  $\delta_f$  is the bending stress,  $P$  is the maximum load,  $L$  is the span,  $b$  is the sample width, and  $d$  is the sample thickness. The calculated maximum bending stress (bending strength) of BiSeI is 16.37 MPa, which is two orders of magnitude smaller than that (1032 MPa) of polycrystalline copper (Cu). Bending strength reflects the ability of materials to resist bending deformation; a smaller bending strength indicates higher susceptibility to bending, meaning a lower rigidity. The inset in Figure 2A shows an optical photograph of the BiSeI sample after the bending test. Despite substantial bending, the BiSeI sample maintains its integrity without visible fractures or cracks.

Nanoindentation tests further demonstrate that the BiSeI is unusually soft. In comparison with polycrystalline Cu (Figure 2B, yellow curve), a typical plastic material, the force-displacement curve of BiSeI (Figure 2B, blue curve) is also smooth and rounded without noticeable pop-in effect. To ensure the reliability of results, the nanoindentation tests were conducted on BiSeI for six times. The average Young's modulus (Figure S4A) of BiSeI is approximately 5.78 GPa, significantly smaller than the 145 GPa of polycrystalline Cu. The lower hardness (Figure S4B) of BiSeI single crystals is around 0.889 GPa. As shown in Figure S5, the SEM was used to observe the indentation after compression by the indenter. The indentations on BiSeI and Cu show no cracks, unlike that on Si, confirming that the BiSeI exhibits substantial capability of plastic deformation and is suitable for the applications of flexible devices.

In contrast, the Bi<sub>2</sub>Se<sub>3</sub> composed of similar elements is a brittle<sup>27</sup> two-dimensional (2D) layered material, which would be fractured layer-by-layer (Inset of Figure S6D) during the nanoindentation test, leading to a pronounced pop-in effect in the force-displacement curve (Figure S6C). The difference in mechanical properties arises from the structural discrepancy between BiSeI and Bi<sub>2</sub>Se<sub>3</sub>. The introduction of iodine (I) causes the material transformation from a 2D structure (Bi<sub>2</sub>Se<sub>3</sub>, Figure S6B) into a quasi-1D structure (BiSeI, Figure S6A), endowing it with more slip planes. The reduction in structure dimension of materials typically alters the physical properties<sup>39-41</sup>, such as Young's modulus. The findings from nanoindentation tests fully support

this trend. The average Young's modulus (Figure S6D) for the 2D Bi<sub>2</sub>Se<sub>3</sub> is 36.5 GPa, while it is only 6.38 GPa for the quasi-1D BiSeI. This reduction in the Young's modulus reflects a decrease in material rigidity, making it more deformable. The reduced Young's modulus of BiSeI infers the superiority of quasi-1D or 1D structure for the design and utilization of new plastic inorganic materials.

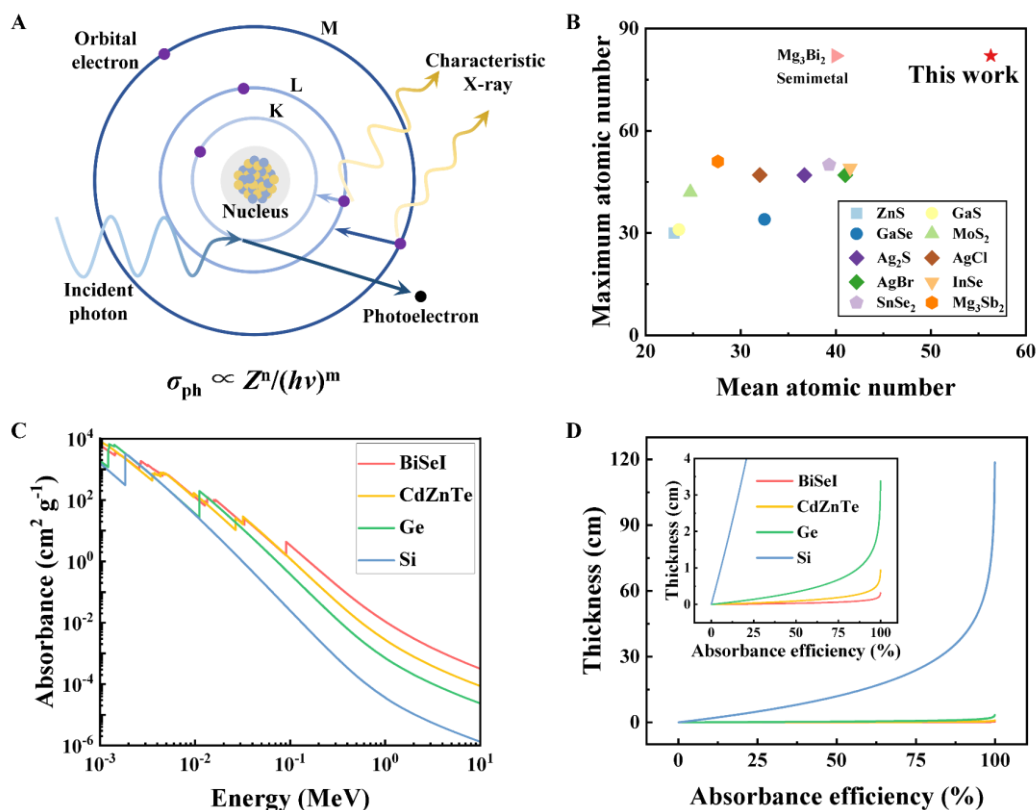


**Fig. 3.** X-ray attenuation ability of BiSeI single crystal. (A) Schematic diagram of the photoelectric effect. (B) Comparison of the atomic numbers ( $Z$  values) of plastic inorganic materials, where the horizontal and vertical coordinates represent the mean and maximum atomic numbers, respectively. (C) Comparison of the absorption coefficient of BiSeI with those of other typical radiation detection materials (CdZnTe, Ge, and Si) calculated by the NIST XCOM database. (D) Thicknesses of BiSeI, CdZnTe, Ge, and Si semiconductors versus their absorbance efficiencies for 0.1 MeV X-ray photons.

There are three primary mechanisms<sup>42</sup> for the interaction of X/ $\gamma$  photons with matter: the photoelectric effect, the Compton scattering, and the electron-pair effect. The photoelectric effect (also known as photoelectric absorption) is depicted in Figure 3A. The probability of the photoelectric effect occurring as the photons interact with matter is expressed by the photoelectric cross-section ( $\sigma_{ph}$ ). This cross-section depends on the incident energy of photons ( $h\nu$ ) and the atomic number ( $Z$ ) of absorbing materials. In general, the  $\sigma_{ph}$  decreases as the  $h\nu$  is increased, while it sharply increases with the  $Z$  of materials. This relationship could be described by the following equation<sup>43</sup>:

$$\sigma_{\text{ph}} \propto \frac{Z^n}{(h\nu)^m} \quad (2)$$

where  $\sigma_{\text{ph}}$  is the photoelectric cross-section,  $Z$  is the atomic number,  $h$  is the Planck's constant,  $\nu$  is the frequency of photons,  $n$  and  $m$  are powers that vary with the photon energy, and  $h\nu$  represents photon energy. Hence the high- $Z$  materials are often preferred to be used for the radiation detectors to achieve higher X/ $\gamma$  detection efficiency. As shown in Figure 3B, the BiSeI has the highest atomic number among the plastic inorganic semiconductors developed currently. Due to its high atomic number, the photoelectric absorption coefficient of BiSeI (Figure 3C) is significantly higher than those of commercial materials such as Si, Ge, and CdZnTe at the photon energy above 0.1 MeV. At the photon energy of 0.1 MeV, the required thicknesses to achieve the X/ $\gamma$  ray attenuation of 99.9% is 118 cm for Si, 3.38 cm for Ge, and 0.944 cm for CdZnTe, whereas it is only 0.317 cm for BiSeI (Figure 3D). This indicates that the radiation detectors based on BiSeI are not only more efficient but also more lightweight, making them ideal for the application of portable devices. Furthermore, the smaller and lighter detectors would offer significant advantages in terms of energy consumption. These features demonstrate the potential of BiSeI for the portable nuclear physics research, miniaturized and flexible medical devices, and aerospace applications.

In addition to a high  $Z$  value, a suitable radiation detection material must exhibit a high  $\mu\tau$  product and a large resistivity. The  $\mu\tau$  product is a key figure of merit for the efficient collection of radiation-induced carriers and can be evaluated using the single-carrier Hecht model<sup>44-46</sup>:

$$\text{CCE} = \frac{\mu\tau V}{d^2} \left[ 1 - e^{\left(\frac{-d^2}{\mu\tau V}\right)} \right] \quad (3)$$

where CCE is the charge collection efficiency,  $V$  is the applied bias,  $d$  is the electrode distance (250  $\mu\text{m}$ ), and  $\mu\tau$  is the product of carrier mobility ( $\mu$ ) and lifetime ( $\tau$ ). The charge collection efficiency is not directly measurable, but it can be generally obtained using the normalization of the number of actual peak channel in the energy spectrum divided by the number of saturated one. The BiSeI-based  $\alpha$ -ray spectrometer can precisely detect the Am-241  $\alpha$ -ray (5485.56 keV) at room temperature and vacuum environment (0.1 Pa) under varying bias voltages from 6 to 60 V as shown in Figure S7A. It is possible that due to the strong penetrating power of gamma rays, the gamma signals of Am-241 and Co-60 were not detected. The optimal energy resolution of 17.6% could be achieved and the  $\alpha$ -ray spectra shift towards higher channel numbers as the applied voltage is increased, indicating the improved charge collection efficiency. Figure S7B shows the fitted charge collection efficiency as a function of bias voltage based on the Hecht model, calculating the  $\mu\tau$  product of BiSeI as  $1.7 \times 10^{-4} \text{ cm}^2 \text{ V}^{-1}$ . This value far exceeds that of a-Se<sup>47,48</sup>, the material currently used in commercial imagers, and is comparable to those of some emerging perovskite



materials<sup>49</sup>. The inset of Figure S7B shows the device structure used for the testing. Given that  $\alpha$  particles from Rn pollution are the significant source of radiation exposure<sup>50</sup>, leading to the lung cancer, this BiSeI-based spectrometer has highly commercial potential for the portable Rn detection.

The resistivity of BiSeI in the b-axis direction measured by the direct current (DC) resistance method is approximately 26.5  $\Omega$  cm (Figure S8), which is similar to the previous reported result<sup>51</sup>. This is even lower than the resistivity of high-purity Ge<sup>52,53</sup> ( $10^2$ - $10^3$   $\Omega$  cm). While the resistivity of BiSeI could be further enhanced by doping in the future. For example, the doping of lower-period chalcogens (S) or halogens (Br, Cl) could increase the bandgap of BiSeI<sup>36,54</sup>. Although the theoretical bandgap of BiSeI is 1.57 eV, the experimental value is 1.34 eV (Figure S9) determined by the photoluminescence (PL) spectroscopy. This discrepancy may be due to the absence of thermal effects<sup>55</sup>, such as lattice expansion and electron-phonon coupling, during the calculation. In general, wide band-gap semiconductors are beneficial to enhance radiation hardness and resistivity, but not conducive to reducing exciton creation energy.<sup>1</sup> At present, many studies<sup>56-58</sup> are one-sidedly focused on increasing the band-gap, while neglecting the attention to the exciton creation energy of the radiation materials. This leads to the shortcomings of most reported X-ray detectors, such as low response current and high energy consumption. Therefore, a smaller bandgap material sometimes may not be a bad choice for radiation detection as the trade-off between the exciton creation energy and the capability of radiation hardness is considered. A comparison of the  $Z$  value,  $\mu\tau$  product, resistivity and flexibility of BiSeI with other classical radiation detection materials (including high-purity Ge, CdZnTe, and MAPbI<sub>3</sub> perovskite) is summarized in the radar chart (Figure S10) and Table S1. The  $\mu\tau$  product of BiSeI is intermediate compared to those of the classical materials, while its resistivity still needs to be increased. BiSeI possesses the highest  $Z$  value and flexible characteristic, far surpassing other radiation detection materials. The excellent flexibility and semiconducting properties of BiSeI make it particularly suitable for the portable and deformable radiation detectors.

The XPS survey (Figure 4A) reveals that the atomic ratio of Bi, Se, and I in BiSeI is approximately 9.3:9.5:10, which closely aligns with the theoretical 1:1:1 ratio as the experimental error is considered. This result implies the high crystal quality of BiSeI. Due to the superior crystallinity of BiSeI single crystals, the photodetectors based on the device structure of metal/BiSeI/metal do not exhibit significant memory phenomenon.<sup>37,59</sup> To introduce the memory functionality, a 50 nm-thick layer of NiO-V<sub>Ni</sub> was deposited onto the BiSeI single crystal by using electron beam evaporation. NiO is a P-type material capable of forming a P-N junction with N-type BiSeI. The atomic ratio of Ni and O in the evaporated NiO layer is 6.9:10 (Figure 4B), significantly deviating from the stoichiometric 1:1 ratio, indicating the formation of a substantial number of Ni vacancies. Raman spectroscopy further supports the presence of Ni vacancies. As shown in Figure 4C, the Raman spectrum of electron beam-evaporated NiO film (yellow) differ significantly from that of commercial

polycrystalline bulk NiO (green). The latter displays one prominent peak near 545  $\text{cm}^{-1}$ , corresponding to the one-phonon first-order longitudinal-optical (1P LO) vibration. In contrast, the former exhibits a significant attenuation of the 1P LO peak and quenching of other Raman peaks, indicating excess defects caused by the Ni vacancies. These defects disrupt the vibrational modes, reducing the intensity and resolution of Raman peaks. The presence of Ni vacancies enables the devices exhibiting the persistent photoconductivity effects as the NiO- $V_{\text{Ni}}$  is integrated with BiSeI.

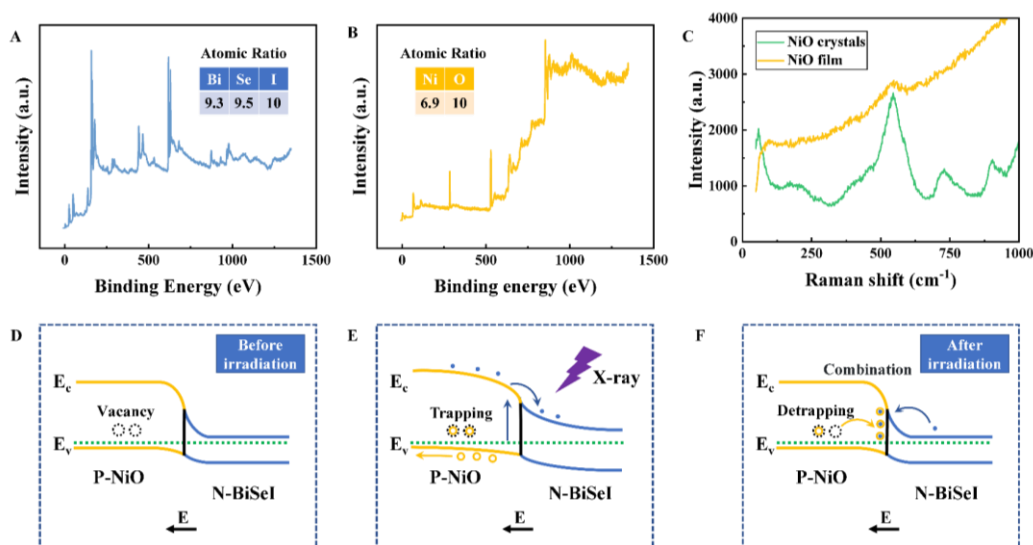


**Fig. 4.** Memory mechanism of the BiSeI/NiO- $V_{\text{Ni}}$  X-ray synaptic devices. (A) (B) XPS survey spectra with the atomic ratios in BiSeI and NiO- $V_{\text{Ni}}$ , respectively. (C) Raman spectrum of NiO crystals and NiO film grown by electron beam deposition. Energy band diagrams of the BiSeI/NiO- $V_{\text{Ni}}$  X-ray synaptic devices (D) before X-ray irradiation, (E) under X-ray irradiation, and (F) after X-ray irradiation.

To investigate the band alignment of the BiSeI/NiO- $V_{\text{Ni}}$  heterostructure, the PL (Figure S9) and optical absorption (Figure S11) measurements were conducted. The bandgap of BiSeI was previously determined to be 1.34 eV. For the NiO- $V_{\text{Ni}}$  film deposited on a quartz substrate, the UV-visible absorption spectrum shows a cutoff wavelength of 362 nm, corresponding to an optical bandgap of approximately 3.42 eV calculated using the Tauc formula<sup>60</sup>. The Kelvin probe force microscopy (KPFM, Figure S12) was used to determine the Fermi level positions of BiSeI and NiO- $V_{\text{Ni}}$ . Based on these results and previous literature studies<sup>55,61</sup>, the energy band diagram of the BiSeI/NiO- $V_{\text{Ni}}$  heterojunction was constructed (Figure S13), revealing a type-II band alignment. This configuration promotes the separation of photogenerated carriers, thereby enhancing the photoelectric response.

Before the X-ray irradiation (Figure 4D), the Fermi levels of BiSeI and NiO- $V_{\text{Ni}}$  align at the P-N junction, resulting in the band bending. The blue and yellow regions represent BiSeI and NiO- $V_{\text{Ni}}$ , respectively. Due to the diffusion of free carriers, a

built-in electric field is formed from BiSeI to NiO-V<sub>Ni</sub>, which is defined as the initial state. During the X-ray irradiation, the BiSeI/NiO-V<sub>Ni</sub> active layer absorbs photons to generate excitons, which diffuse towards the P-N junction. The excitons in NiO-V<sub>Ni</sub> transfer electrons to BiSeI, while the excitons in BiSeI transfer holes to NiO-V<sub>Ni</sub>, enabling effective charge separation. The electrons and holes migrate to the negative and positive electrodes through BiSeI and NiO-V<sub>Ni</sub>, respectively, generating a photocurrent. This process flattens the energy band, compared to that before irradiation (Figure 4E).

As the irradiation is continued, a large number of photogenerated carriers accumulate at the BiSeI/NiO-V<sub>Ni</sub> interface. Some photogenerated holes are captured by the Ni vacancies, causing the excitatory postsynaptic current (EPSC) to increase with prolonged irradiation. After the irradiation is ceased (Figure 4F), the photogenerated electrons begin to recombine with holes, reducing the EPSC. However, the holes trapped by Ni vacancies delay the recombination, resulting in a gradual decrease of current and a bent energy band. This persistent current demonstrates the memory function of BiSeI/NiO-V<sub>Ni</sub> heterojunction, mimicking the optical synapse behavior.

The conduction state of device is regulated by the Ni vacancies in NiO-V<sub>Ni</sub>, while the BiSeI primarily governs the X-ray absorption. These two materials synergistically enable the processes of photon absorption, exciton generation, charge separation, hole trapping, and gradual carrier release, highlighting the potential of BiSeI/NiO-V<sub>Ni</sub> devices for advanced photoelectric applications. Figure 5A illustrates a diagram of both a biological synapse and a BiSeI/NiO-V<sub>Ni</sub> double-ended X-ray synaptic device (see Figure S14 for the physical device image). In the biological synapses, the presynaptic membrane, synaptic cleft, and postsynaptic membrane are the fundamental components involved in visual perception and information transmission. When an action potential is triggered, the presynaptic membrane releases neurotransmitters to either excite or inhibit the postsynaptic neuron. In the device configuration, the source electrode (Ag) and leakage electrode (Au) serve as the presynaptic and postsynaptic membranes, respectively. The X-ray pulse is analogous to an action potential, while the BiSeI/NiO-V<sub>Ni</sub> functions as the neurotransmitter and the increase in conductance induced by the X-ray stimulation is equivalent to the EPSC.

Synaptic plasticity, which encompasses both short-term plasticity (STP) and long-term plasticity (LTP), is the key feature of biological synapses and is closely related to the crucial life functions such as memory, learning, and adaptation. The STP, associated with short-term memory (STM), typically lasts for a few seconds, while the LTP, which refers to the enhanced connectivity between neurons and corresponds to long-term memory (LTM) that can persist for over 100 seconds<sup>62</sup>, makes synaptic transmission more effective. The paired-pulse facilitation (PPF), a phenomenon associated with STP, occurs as a preceding stimulus enhances the subsequent synaptic response. The X-ray synaptic device reported here successfully

mimics this behavior. The inset of Figure 5B demonstrates the EPSC response of the BiSeI/NiO-V<sub>Ni</sub> synaptic device, induced by two consecutive X-ray pulses spaced 1 s apart with a pulse width of 5 s at a dose rate of 1357 nGy s<sup>-1</sup>. The second EPSC ( $P_2$ ) generated by the second pulse is greater than the first one ( $P_1$ ) as the photogenerated electron-hole pairs from the first pulse are not fully recombined before the second pulse, which is consistent with the PPF observed in the biological synapses. The relationship between the PPF index ( $P_2/P_1 \times 100\%$ ) and the time interval between pulses (Figure 5B) is well fitted by the following equation<sup>63</sup>:

$$PPF \text{ index} = A_0 + A_1 \exp(-\Delta t/\tau_1) + A_2 \exp(-\Delta t/\tau_2) \quad (4)$$

Here,  $\Delta t$  is the interval time between the two spikes,  $A_1$  and  $A_2$  are the initial magnitudes of facilitation, as well as  $t_1$  and  $t_2$  separately represent the rapid and slow relaxation time constants. In this study,  $\tau_1=0.08$  s and  $\tau_2=5.66$  s, with  $\tau_2$  being approximately one order of magnitude larger than  $\tau_1$ , which is similar to the behavior of biological synapses.<sup>64</sup> The PPF index is inversely proportional to the time interval, where a longer interval results in a smaller  $P_2$ , thereby reducing the PPF.

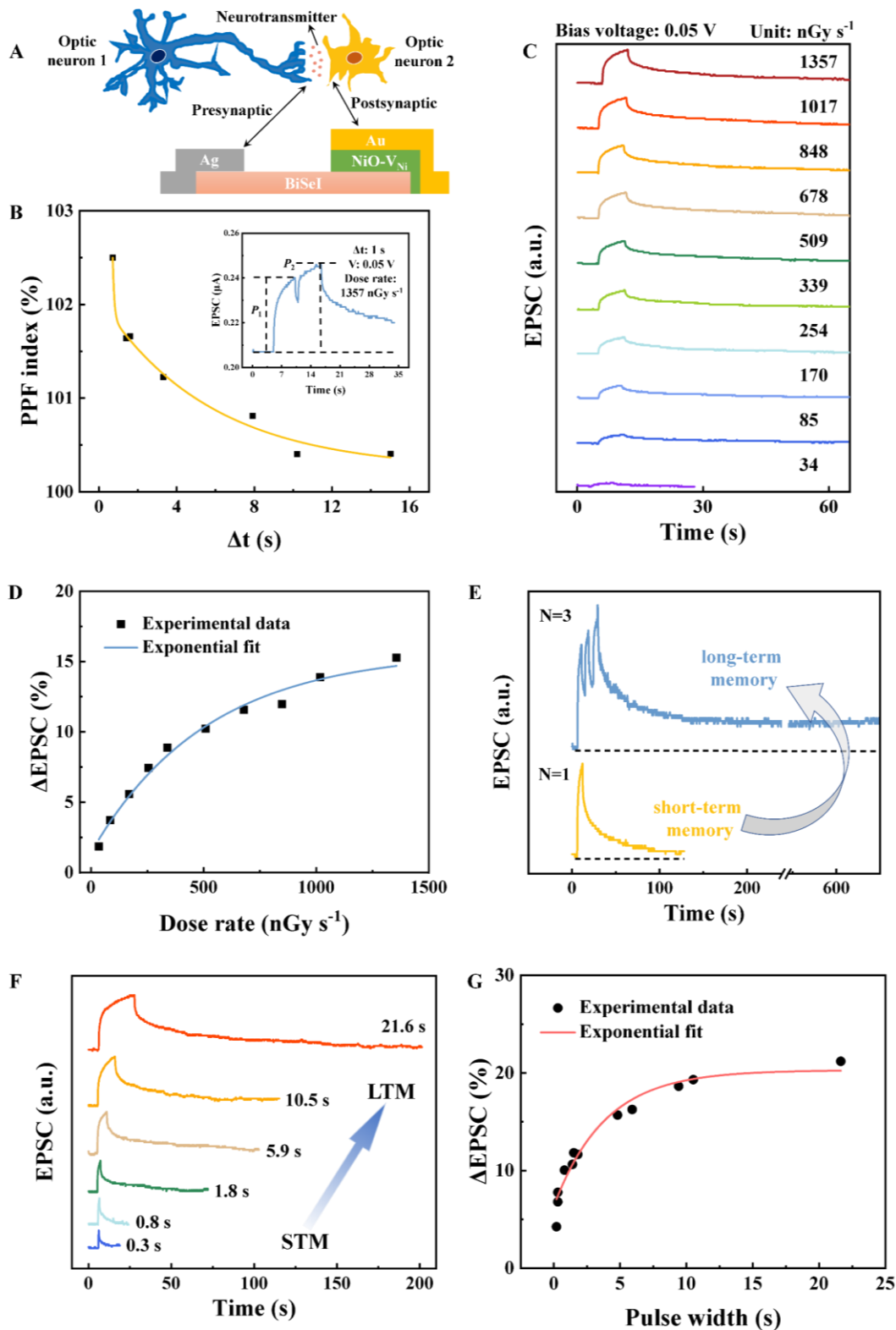
To facilitate the synaptic functionality, the device must perform the STP, LTP, and their interconversion through modulation of stimulation intensity. The synaptic plasticity of the BiSeI/NiO-V<sub>Ni</sub> X-ray synaptic device can be systematically studied by varying the parameters of X-ray pulse, such as dose rate, pulse number, and pulse width.

Figure 5C shows the photocurrents of device caused by the single X-ray pulse (pulse width of 5 s) with different dose rates. At higher dose rates, more charge carriers are generated, leading to a higher EPSC, which is analogous to the behavior of biological synapses. The dose rate varying from 34 to 1357 nGy s<sup>-1</sup> achieves a typical transition from STP to LTP, indicating the ability of device to mimic the synaptic plasticity. Notably, the BiSeI/NiO-V<sub>Ni</sub> detectors exhibited an ultralow detection limit of 34 nGy s<sup>-1</sup>, about 1/1288 dose rate of the commercial medical chest X-ray diagnosis. And the applied regulatory voltage ( $V_{DS} = 0.05$  V) is only half<sup>65</sup> of the typical voltage in the biological systems, indicating an advantage of low power consumption for our device. The power consumption ( $E$ ) can be quantified by the following equation<sup>64</sup>:

$$E = I \times V \times t \quad (5)$$

where  $I$  is the difference between the photocurrent and the dark current,  $V$  is the operating voltage, and  $t$  is the duration of irradiation pulse (pulse width). A smaller applied voltage results in reduced power consumption. The ideal synaptic device should reach the power consumption level of biological synapses. However, the research on X-ray synapses is still in its infancy. In this study, the result is already at the leading level among the current researches of X-ray synapse<sup>1,3,66</sup> (Figure S16), although the power consumption per spike ( $\sim 90$  pJ, 0.2 s irradiation at 1357 nGy s<sup>-1</sup>,

Figure S15) of the BiSeI/NiO-V<sub>Ni</sub> synaptic device cannot be compared with that of biological synapses (1~100 fJ)<sup>67</sup>.



**Fig. 5.** Performance of the BiSeI/NiO-V<sub>Ni</sub> X-ray synaptic devices. (A) Schematic diagram of the information transmission related to the visual nerves and the BiSeI/NiO-V<sub>Ni</sub> X-ray synaptic devices. (B) The PPF index as a function of interval time ( $\Delta t$ ). Inset: The PPF behavior of irradiation synaptic

devices at an interval time of 1 s and a pulse width of 5 s (dose rate: 1357 nGy s<sup>-1</sup>, bias voltage: 0.05 V). (C) The photocurrent of BiSeI/NiO-V<sub>Ni</sub> X-ray synaptic devices under the irradiation with different dose rates at 0.05 V for 5 s. (D) Synaptic weight ( $\Delta EPSC$ ) variation as a function of X-ray dose rate. (E) STM and LTM are controlled by the irradiation pulses with different pulse numbers under 1357 nGy s<sup>-1</sup> at 0.05 V. (F) Dependence of the photocurrent of BiSeI/NiO-V<sub>Ni</sub> X-ray synaptic devices on different irradiation durations with the dose rate of 1357 nGy s<sup>-1</sup> at 0.05 V. (G) The  $\Delta EPSC$  as a function of irradiation duration.

To quantify the influence of dose rates on EPSC, we performed the calculations and functional simulations of  $\Delta EPSC$  as shown in Figure 5D. The  $\Delta EPSC$  representing the synaptic weight is defined as the ratio of  $(I_{\text{irrad}} - I_{\text{dark}})/I_{\text{dark}}$ , where  $I_{\text{dark}}$  is the current without irradiation and  $I_{\text{irrad}}$  is the photocurrent during irradiation. In the BiSeI/NiO-V<sub>Ni</sub> synapse device, the conductance of BiSeI/NiO-V<sub>Ni</sub> is considered as the synaptic weight, the photon stimulus is regarded as a presynaptic spike, and the drain current of device is functionalized as the postsynaptic current. The relationship between the dose rate and  $\Delta EPSC$  follows the equation as below<sup>68</sup>:

$$\Delta EPSC = y_0 + y_1 \exp(-x/t) \quad (6)$$

where  $y_0$  is the resting facilitation amplitude,  $y_1$  is the initial facilitation amplitude during training,  $x$  is the dose rate, and  $t$  represents the facilitation magnitude of presynaptic spikes. This equation indicates a positive correlation between the dose rates and  $\Delta EPSC$ , reflecting that the stronger stimulation results in the higher memory retention. With the increase of learning intensity (radiation dose rate), the  $\Delta EPSC$  is increased from 1.85 to 15.3% and then gradually saturated, revealing that the synaptic weights are adjustable. Meanwhile, the LTP is eventually realized.

The memory characteristic of the X-ray synaptic device can also be modulated by the number of irradiation pulses. Figure 5E presents the EPSC for one-pulse and three-pulse radiations (pulse width of 5 s and time interval of 5 s) at 1357 nGy s<sup>-1</sup>. The recombination times of photogenerated electron-hole pairs have been increased from about 100 s to 650 s by increasing the number of pulses, which demonstrates the transition from STP to LTP in the device.

As shown in Figure 5F, the duration of irradiation pulses (pulses width) can also serve as a parameter to adjust the synaptic behavior of device. The EPSC increases with the irradiation duration, which is consistent with previous studies<sup>69-71</sup> on the infrared/visible/ultraviolet synapses. The BiSeI/NiO-V<sub>Ni</sub> synaptic device achieves typical transition from STP to LTP under continuous irradiation (1357 nGy s<sup>-1</sup>) from 0.3 s to 21.6 s. The carrier recombination time is extended from tens to hundreds of seconds, demonstrating the ability of device to emulate the synaptic plasticity. Figure 5G shows the evolution of  $\Delta EPSC$  with irradiation time, suggesting that the connectivity between synapses increases and approaches saturation as the irradiation time is increased. The amount of separated electron-hole pairs is gradually balanced by the recombination as the illumination time is extended, resulting in an increase of

$\Delta EPSC$  from 4.25 to 21.2%. The experimental data could be closely fitted by the equation as below:

$$\Delta EPSC = y_0 + y_1 \exp(-w/t) \quad (7)$$

where  $y_0$  represents the resting facilitation amplitude,  $y_1$  represents the initial facilitation magnitude during training,  $w$  is the duration of presynaptic spike, and  $t$  denotes the facilitation magnitude of presynaptic spikes. The performance of BiSeI/NiO- $V_{Ni}$  synaptic device is consistent with the basic synaptic behavior as well as the visual models of human memory and forgetting, demonstrating its great application prospects for advanced and intelligent X-ray detection systems.

Moreover, the response sensitivity of the BiSeI/NiO- $V_{Ni}$  synaptic device is also related to the irradiation time, which is similar to the conclusion in previous literature<sup>1</sup>. Unlike the classic X-ray photoelectric detectors, the photocurrent gain ( $I_{irrad}-I_{dark}$ ) of the X-ray synapse is increased with the irradiation time. Therefore, when defining the X-ray induced current density and calculating the sensitivity, it is necessary to study the photocurrent gain of the X-ray synapse for different irradiation times. As shown in Figure 6A, the data extracted from Figure 5C under irradiation for 0.3 s shows that the X-ray induced current density is approximately linearly related to the dose rate. The slope of the fitted curve represents the sensitivity of detector, which is calculated to be  $1,346,690 \mu C Gy_{air}^{-1} cm^{-2}$ , surpassing most of flexible devices and even being comparable to the performance of some perovskite single crystals (Figure 6B and Table S2). However, the data extracted from Figure 5C under irradiation for 3 s shows an exponential relationship. Clearly, the relationship between the photocurrent gain density and the dose rate can be changed by different irradiation times, further demonstrating the plasticity of the BiSeI/NiO- $V_{Ni}$  X-ray synapse.

Finally, we verified the cyclic bending stability of the device under a curvature radius of 5 mm. Under an X-ray pulse with a dose rate of  $1357 nGy s^{-1}$  and an irradiation time of 0.8 s, the photocurrent variation over time of the BiSeI/NiO- $V_{Ni}$  synaptic device after 0, 25, and 50 cycles of bending and flattening, as well as when maintained in a bent state, is shown in Figure S17. The ESPC of the device changes hardly in value, but the recombination time of carriers is prolonged since the bending causes the formation of more dislocation defects. This is an interesting method and idea for improving the memory time.

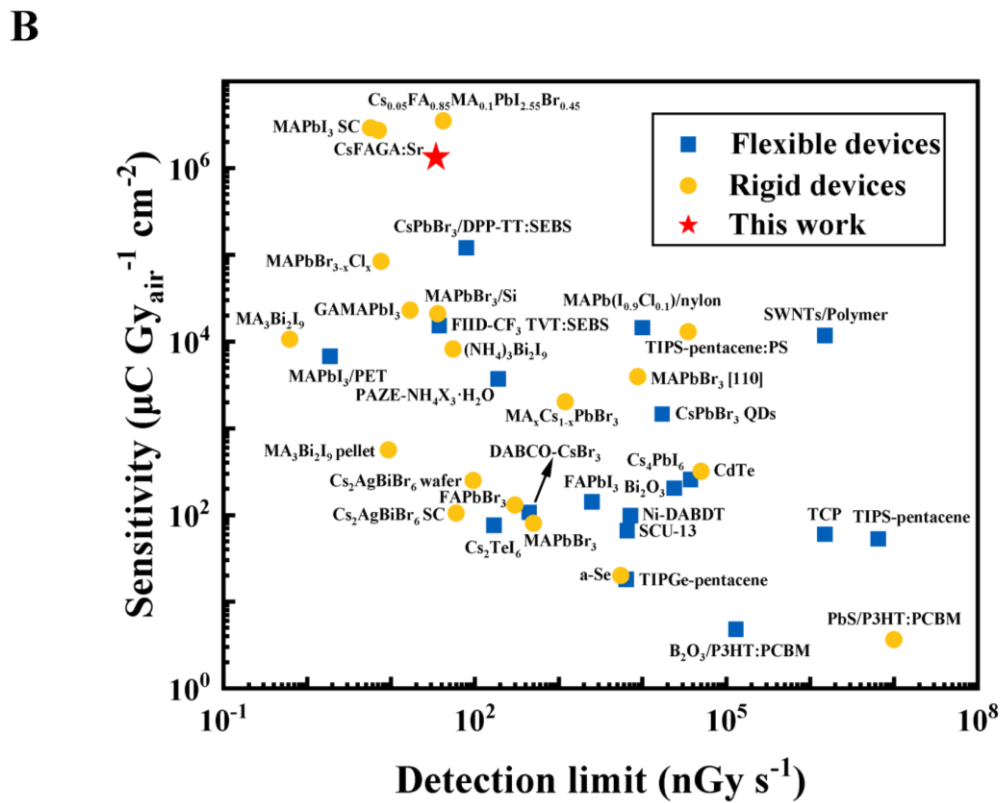
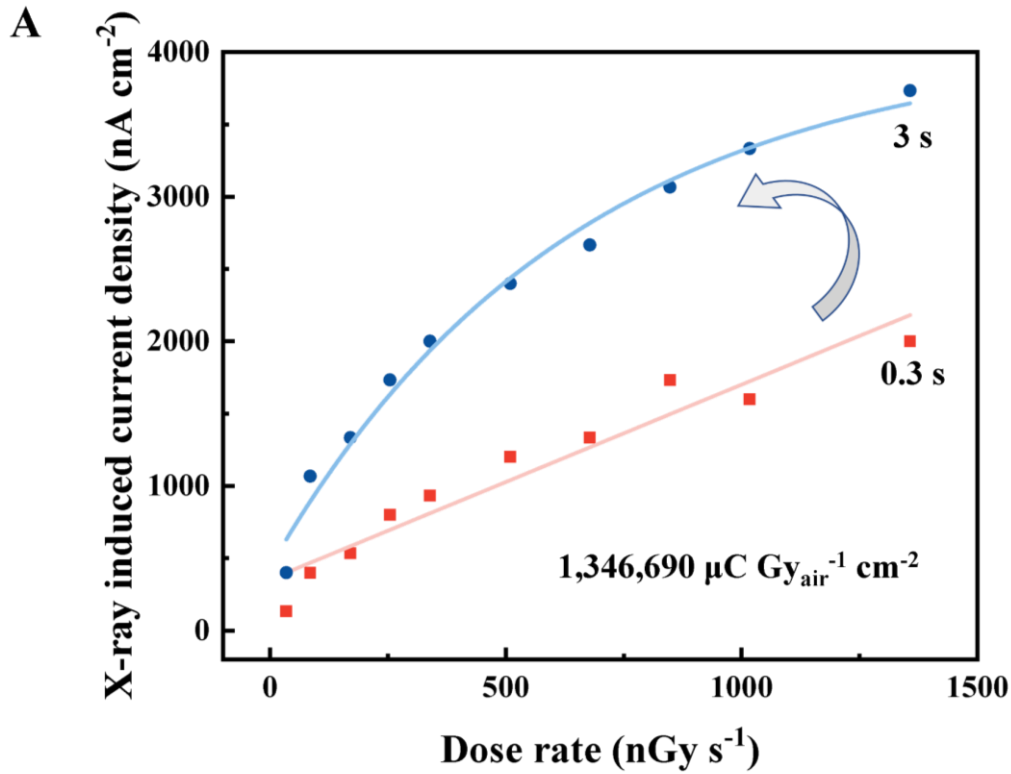


**Fig. 6.** Performance characteristics and advantages of the BiSeI/NiO- $V_{\text{Ni}}$  X-ray synapses. (A) The photocurrent density of BiSeI/NiO- $V_{\text{Ni}}$  X-ray synapses induced by the X-ray irradiation for 0.3 and 3 s as a function of dose rate from 34 to 1357  $\text{nGy s}^{-1}$ . (B) The sensitivities and detection limits of currently reported X-ray detectors and the BiSeI/NiO- $V_{\text{Ni}}$  X-ray synapses in this work.



## Conclusions

In this work, the BiSeI/NiO-V<sub>Ni</sub> outperforms the conventional materials such as Si, Ge, and CdZnTe in terms of photon absorption, allowing for thinner and more lightweight X-ray detectors. Its excellent mechanical flexibility makes it ideal for in the application of flexible and portable devices. This characteristic is particularly important for the development of next-generation X-ray detectors applied to aerospace, wearable medical devices, and environmental monitoring systems. Another key feature of BiSeI/NiO-V<sub>Ni</sub> is its ability to mimic the synaptic plasticity as it is integrated into X-ray synaptic devices, which can emulate the function of biological synapses. This capability allows for the creation of devices which can not only detect X-rays but also exhibit memory-like behaviors, such as STP and LTP. The synaptic behavior of BiSeI/NiO-V<sub>Ni</sub> devices can be tuned by adjusting the irradiation parameters to simulate STM LTM, offering new avenues for the bio-inspired radiation detection systems. These devices can mimic the learning and adaptive capabilities of the human nervous system, which is crucial for improving the accuracy and sensitivity of X-ray detection in various applications.

In summary, this work highlights the potential of BiSeI/NiO-V<sub>Ni</sub> as a leading material for the next-generation of flexible and efficient X-ray detectors. The unique combination of high photoelectric absorption coefficient, excellent flexibility, and synaptic memory capability sets BiSeI/NiO-V<sub>Ni</sub> device apart from traditional detectors, overcoming the current challenges in the industry of X-ray detection. The advancements made in this study open up exciting possibilities for the portable, low-power, and high-performance X-ray detection technologies, paving the way for innovative applications in medical, environmental, and industrial fields.

## Methods

**Characterization.** The initial sample dimension for three points bending is 15×3×0.25 mm<sup>3</sup>, using Instron-5969 universal testing machine with a constant loading rate of 0.05 mm min<sup>-1</sup>. Nanoindentation data were collected on Agilent G200. The scanning electron microscope (SEM) images were carried out on ZEISS Merlin Compact. Optical photographs were taken by VIVO IQOO Z7I. Resistivity test was recorded by Keithley 2400 using a dc resistance method. The Raman spectra and PL spectrum was obtained by using Renishaw inVia Raman microscope with a 532 nm excitation wavelength at room temperature. The BiSeI crystal was examined by X-ray diffraction using Cu K $\alpha$  Source (Panalytical Instruments, X'PERT). The absorption coefficients were calculated using the NIST Photon Cross Section Database (XCOM). The X-rays tube was manufactured by Source-Ray, Inc (Model SB-80-500). The X-ray source operated at an accelerating voltage of 50 kV, and the dose rate was adjusted by changing the tube current (10  $\mu$ A–400  $\mu$ A). The  $\alpha$ -ray spectroscopies were operated coupled with ORTEC system (preamplifier 142B, main amplifier 572A and multichannel pulse analyzer EASY-MCA), generated by 241Am  $\alpha$ -ray radiation (5485.56 keV, activity 0.06 MBq). The Kelvin probe force microscopy (KPFM) dates were tested by Dimension FastScan<sup>®</sup> Atomic force microscope (AFM). The XPS surveys were revealed by X-ray photoelectron spectroscopy (XPS) ESCALAB 250Xi. The UV-visible absorption spectrum was determined by PerkinElmer Lambda 950 ultraviolet-visible spectrophotometer.

### Device fabrication.

High-purity Au (4N, 99.99%), Ag (4N, 99.99%), Bi (5N, 99.999%), Se (5N, 99.999%), I (4N, 99.99%), NiO (3N, 99.9%) and MoO<sub>3</sub> (4N, 99.99%) were obtained from ZhongNuo Advanced Material (Beijing) Technology Co., Ltd, and used as the raw materials.

The structure of the X-ray synaptic device is Au/NiO-V<sub>Ni</sub>/BiSeI/Ag, where BiSeI crystal is obtained by CVT process in the main text and the thickness is 0.25 mm. The NiO-V<sub>Ni</sub> film (50 nm) was prepared by electron beam evaporation. The Au and Ag electrodes were deposited by thermal evaporation with a thickness of 100 nm, and the Au/Ag electrodes were coated with conductive graphite and silver adhesives, respectively, for follow-up tests. The channel length and width of the device are 1 and 3 mm respectively. The entire device is attached to a flexible PET substrate by 3M™ 100MP high performance acrylic adhesive (F9460PC). To ensure the accuracy of the data, there is a tungsten shield with a 1×3 mm<sup>2</sup> slit between the device and the X-ray source.

The structure of the  $\alpha$ -ray spectrometer is Au/Cr/MoO<sub>3</sub>/BiSeI/Ag, where the distance between the Cr/Au electrodes (10/100 nm) and the Ag electrode (100 nm) is 250  $\mu$ m. MoO<sub>3</sub> (50 nm) acts as a buffer layer for hole modification, which is evaporated by electron beam.

### Data availability

The data that support the findings of this study are available from the corresponding authors upon reasonable request.

### References

1. Liang, H. *et al.* Retina-Inspired X-Ray Optoelectronic Synapse Using Amorphous Ga<sub>2</sub>O<sub>3</sub> Thin Film. *Advanced Science* **2410761**, 1–11 (2024).
2. Liu, Y. *et al.* Reservoir Computing Based on Oxygen-Vacancy-Mediated X-ray Optical Synaptic Device for Medical CT Bone Diagnosis. *ACS Applied Materials & Interfaces* **16**, 24871–24878 (2024).
3. Yin, H. *et al.* Retinomorph X-ray detection using perovskite with hydron-conductive organic cations. *Innovation* **5**, 100654 (2024).
4. Barba, P. *et al.* Remote telesurgery in humans: a systematic review. *Surgical Endoscopy* **36**, 2771–2777 (2022).
5. He, Y. *et al.* Perovskite computed tomography imager and three-dimensional reconstruction. *Nature Photonics* **18**, (2024).
6. Hua, Y. *et al.* Suppressed ion migration for high-performance X-ray detectors based on atmosphere-controlled EFG-grown perovskite CsPbBr<sub>3</sub> single crystals. *Nature Photonics* **18**, 870–877 (2024).
7. Liu, L. *et al.* Anti-perovskites with long carrier lifetime for ultralow dose and stable X-ray detection. *Nature Photonics* **18**, 990–997 (2024).
8. Pan, W. *et al.* a Low Detection Limit. *Nature Photonics* **11**, 1–8 (2017).
9. Chen, S. *et al.* Atomic scale insights into structure instability and

- decomposition pathway of methylammonium lead iodide perovskite. *Nature Communications* 1–8 (2018) doi:10.1038/s41467-018-07177-y.
10. Chen, S. *et al.* General Decomposition Pathway of Organic – Inorganic Hybrid Perovskites through an Intermediate Superstructure and its Suppression Mechanism. **2001107**, 1–7 (2020).
  11. Detectors, C. C. *et al.* Ion Migration Controlled Stability in  $\alpha$  - Particle Response of. (2021) doi:10.1021/acs.jpcc.0c10758.
  12. You, A., Be, M. & In, I. Defect proliferation in CsPbBr<sub>3</sub> crystal induced by ion migration . (2023) doi:10.1063/1.5134108.
  13. Zou, H. *et al.* Angular response of ‘pin-hole’ imaging structure measured by collimated  $\beta$  source. *Science China Technological Sciences* **56**, 2675–2680 (2013).
  14. Badawi, M. S. *et al.* Calibration of  $4\pi$  NaI(Tl) detectors with coincidence summing correction using new numerical procedure and ANGLE4 software. *AIP Advances* **7**, 35005 (2017).
  15. Lyu, Z. *et al.* Development and Performance Evaluation of a  $4\pi$  View Radiation Imaging System. in *2019 IEEE Nuclear Science Symposium and Medical Imaging Conference (NSS/MIC)* 1–3 (2019). doi:10.1109/NSS/MIC42101.2019.9059639.
  16. Mingels, C. *et al.* Impact of the new ultra-high sensitivity mode in a long axial field-of-view PET/CT. *Annals of Nuclear Medicine* **37**, 310–315 (2023).
  17. Yoshida, K. & Tadokoro, S. *Field and Service Robotics. Field and Service Robotics* (1998). doi:10.1007/978-1-4471-1273-0.
  18. Mooney, J. G. & Johnson, E. N. A Comparison of Automatic Nap-of-the-earth Guidance Strategies for Helicopters. *Journal of Field Robotics* **30**, 1–17 (2014).
  19. Sato, Y. *et al.* Radiation imaging using a compact Compton camera mounted on a crawler robot inside reactor buildings of Fukushima Daiichi Nuclear Power Station. *Journal of Nuclear Science and Technology* **56**, 801–808 (2019).
  20. Zhan, X., Jiang, Z., Chen, Z., Zhang, M. & Song, C. Structures of GMCW37. *Research in Astronomy and Astrophysics* **14**, 433–455 (2014).
  21. Zhang, X. *et al.* High energy resolution CsPbBr<sub>3</sub> alpha particle detector with a full-customized readout application specific integrated circuit. *Nature Communications* **15**, (2024).
  22. Zhang, Z. *et al.* In-sensor reservoir computing system for latent fingerprint recognition with deep ultraviolet photo-synapses and memristor array. *Nature Communications* **13**, 1–9 (2022).
  23. Jiang, T. *et al.* Tetrachromatic vision-inspired neuromorphic sensors with

- ultraweak ultraviolet detection. *Nature Communications* **14**, (2023).
24. Luo, X. *et al.* A bionic self-driven retinomorph eye with ionogel photosynaptic retina. *Nature Communications* **15**, 1–9 (2024).
  25. Zhang, Z. *et al.* All-in-one two-dimensional retinomorph hardware device for motion detection and recognition. *Nature Nanotechnology* **17**, 27–32 (2022).
  26. Wang, Q. *et al.* Plastic Inorganic van der Waals Semiconductors for Flexible X-ray Detectors. (2025) doi:10.1021/acsaelm.4c01931.
  27. Gao, Z. *et al.* High-throughput screening of 2D van der Waals crystals with plastic deformability. *Nature Communications* **13**, (2022).
  28. Zhao, P. *et al.* Plasticity in single-crystalline Mg<sub>3</sub>Bi<sub>2</sub> thermoelectric material. *Nature* **631**, 777–782 (2024).
  29. Li, A. *et al.* High performance magnesium-based plastic semiconductors for flexible thermoelectrics. *Nature Communications* **15**, (2024).
  30. Deng, T. *et al.* Room-temperature exceptional plasticity in defective Bi<sub>2</sub>Te<sub>3</sub>-based bulk thermoelectric crystals. *Science* **386**, 1112–1117 (2024).
  31. Feng, T. *et al.* Large Transverse and Longitudinal Magneto-Thermoelectric Effect in Polycrystalline Nodal-Line Semimetal Mg<sub>3</sub>Bi<sub>2</sub>. *Advanced Materials* **34**, 2200931 (2022).
  32. Feng, T. *et al.* Giant transverse thermoelectric effect induced by topological transition in polycrystalline Dirac semimetal Mg<sub>3</sub>Bi<sub>2</sub>. *Energy & Environmental Science* **16**, 1560–1568 (2023).
  33. Wei, H. & Huang, J. Halide lead perovskites for ionizing radiation detection. *Nature Communications* **10**, 1–12 (2019).
  34. Dudipala, K. R., Le, T. H., Nie, W. & Hoye, R. L. Z. Halide Perovskites and Their Derivatives for Efficient, High-Resolution Direct Radiation Detection: Design Strategies and Applications. *Advanced Materials* **36**, (2024).
  35. Johns, P. M. & Nino, J. C. Room temperature semiconductor detectors for nuclear security. *Journal of Applied Physics* **126**, (2019).
  36. Ghorpade, U. V. *et al.* Emerging Chalcohalide Materials for Energy Applications. *Chemical Reviews* **123**, 327–378 (2023).
  37. Hu, H. J. *et al.* Enhanced optoelectronic performance and photogating effect in quasi-one-dimensional BiSeI wires. *Applied Physics Letters* **120**, (2022).
  38. Xiao, B. *et al.* Centimeter size BiSeI crystal grown by physical vapor transport method. *Journal of Crystal Growth* vol. 517 7–11 (2019).
  39. Kuchibhatla, S. V. N. T., Karakoti, A. S., Bera, D. & Seal, S. One dimensional nanostructured materials. *Progress in Materials Science* **52**, 699–913 (2007).
  40. Lu, J. G., Chang, P. & Fan, Z. Quasi-one-dimensional metal oxide materials—Synthesis, properties and applications. *Materials Science and*

- Engineering: R: Reports* **52**, 49–91 (2006).
41. Balandin, A. A., Kargar, F., Salguero, T. T. & Lake, R. K. One-dimensional van der Waals quantum materials. *Materials Today* **55**, 74–91 (2022).
  42. Liu, F. *et al.* The working principle of hybrid perovskite gamma-ray photon counter. *Materials Today* **37**, 27–34 (2020).
  43. Evan, R. D. *The Atomic Nucleus*. McGraw-hill New York (1955).
  44. Yakunin, S. *et al.* Detection of gamma photons using solution-grown single crystals of hybrid lead halide perovskites. *Nature Photonics* **10**, 585–589 (2016).
  45. He, Y. *et al.* Resolving the Energy of  $\gamma$ -Ray Photons with MAPbI<sub>3</sub> Single Crystals. *ACS Photonics* **5**, 4132–4138 (2018).
  46. McCall, K. M. *et al.*  $\alpha$ -Particle Detection and Charge Transport Characteristics in the A<sub>3</sub>M<sub>2</sub>I<sub>9</sub> Defect Perovskites (A = Cs, Rb; M = Bi, Sb). *ACS Photonics* **5**, 3748–3762 (2018).
  47. Hunter, D. M., Belev, G., Kasap, S. & J. Yaffe, M. Measured and calculated K-fluorescence effects on the MTF of an amorphous-selenium based CCD x-ray detector. *Medical Physics* **39**, 608–622 (2012).
  48. Kasap, S. O. X-ray sensitivity of photoconductors: Application to stabilized a-Se. *Journal of Physics D: Applied Physics* **33**, 2853–2865 (2000).
  49. Kim, Y. C. *et al.* Printable organometallic perovskite enables large-area, low-dose X-ray imaging. *Nature Publishing Group* **550**, 87–91 (2017).
  50. Kelly DP, S. A. *The New England Journal of Medicine* Downloaded from nejm.org at UNIVERSIDAD DE CHILE on December 15, 2010. For personal use only. No other uses without permission. Copyright © 1994 Massachusetts Medical Society. All rights reserved. (1994).
  51. Bai, R. *et al.* Growth of bismuth- and antimony-based chalcogenide single crystals by the physical vapor transport method. *CrystEngComm* **24**, 1094–1099 (2022).
  52. Owens, A. & Peacock, A. Compound semiconductor radiation detectors. *Nuclear Instruments and Methods in Physics Research Section A: Accelerators, Spectrometers, Detectors and Associated Equipment* **531**, 18–37 (2004).
  53. Yang, G. *et al.* Study on the Properties of High Purity Germanium Crystals. *Journal of Physics: Conference Series* **606**, (2015).
  54. Zhang, F., Chen, W., Zhang, Y. & Yin, H. 1D group V-VI-VII ternary nanowires: moderate band gaps, easy to exfoliate from bulk, and unexpected ferroelectricity. *Physical Chemistry Chemical Physics* **25**, 6112–6120 (2023).
  55. Ganose, A. M., Butler, K. T., Walsh, A. & Scanlon, D. O. Relativistic electronic structure and band alignment of BiSI and BiSeI: Candidate

- photovoltaic materials. *Journal of Materials Chemistry A* **4**, 2060–2068 (2016).
56. Wang, S. *et al.* Crystal Growth of Tl<sub>4</sub>CdI<sub>6</sub>: A Wide Band Gap Semiconductor for Hard Radiation Detection. *Crystal Growth & Design* **14**, 2401–2410 (2014).
  57. Johnsen, S. *et al.* Thallium Chalcogenide-Based Wide-Band-Gap Semiconductors: TlGaSe<sub>2</sub> for Radiation Detectors. *Chemistry of Materials* **23**, 3120–3128 (2011).
  58. Lin, W. *et al.* Cu<sub>2</sub>I<sub>2</sub>Se<sub>6</sub>: A Metal-Inorganic Framework Wide-Bandgap Semiconductor for Photon Detection at Room Temperature. *Journal of the American Chemical Society* **140**, 1894–1899 (2018).
  59. Li, Y. *et al.* Polarization-Sensitive Photodetector Based on High Crystallinity Quasi-1D BiSeI Nanowires Synthesized via Chemical Vapor Deposition. *Small* **19**, 2302623 (2023).
  60. Klein, J. *et al.* Limitations of the Tauc Plot Method. *Advanced Functional Materials* **33**, 1–19 (2023).
  61. Kossar, S., Amiruddin, R. & Rasool, A. Investigation on asymmetric resistive switching (RS) characteristics in p-NiO/n-ZnO heterojunctions. *Microelectronic Engineering* **254**, 111669 (2022).
  62. Li, J. *et al.* Artificial synapses enabled neuromorphic computing: From blueprints to reality. *Nano Energy* **103**, 107744 (2022).
  63. Liu, Y. H., Zhu, L. Q., Feng, P., Shi, Y. & Wan, Q. Freestanding Artificial Synapses Based on Laterally Proton-Coupled Transistors on Chitosan Membranes. *Advanced Materials* **27**, 5599–5604 (2015).
  64. Li, X., Li, S., Tang, B., Liao, J. & Chen, Q. A Vis-SWIR Photonic Synapse with Low Power Consumption Based on WSe<sub>2</sub>/In<sub>2</sub>Se<sub>3</sub> Ferroelectric Heterostructure. *Advanced Electronic Materials* **8**, 1–9 (2022).
  65. Hu, Y. *et al.* Ultralow Power Optical Synapses Based on MoS<sub>2</sub> Layers by Indium-Induced Surface Charge Doping for Biomimetic Eyes. *Advanced Materials* **33**, 1–11 (2021).
  66. Liu, Y. *et al.* Reservoir Computing Based on Oxygen-Vacancy-Mediated X-ray Optical Synaptic Device for Medical CT Bone Diagnosis. *ACS Applied Materials and Interfaces* **16**, 24871–24878 (2024).
  67. Laughlin, S. B., de Ruyter van Steveninck, R. R. & Anderson, J. C. The metabolic cost of neural information. *Nature Neuroscience* **1**, 36–41 (1998).
  68. Yang, Y. *et al.* Long-Term Synaptic Plasticity Emulated in Modified Graphene Oxide Electrolyte Gated IZO-Based Thin-Film Transistors. *ACS Applied Materials & Interfaces* **8**, 30281–30286 (2016).
  69. Wang, J. *et al.* Technology and Integration Roadmap for Optoelectronic Memristor. *Advanced Materials* **36**, 1–47 (2024).

70. Zhao, T. *et al.* Bio-Inspired Photoelectric Artificial Synapse based on Two-Dimensional Ti<sub>3</sub>C<sub>2</sub>T<sub>x</sub> MXenes Floating Gate. *Advanced Functional Materials* **31**, 1–11 (2021).
71. Wang, S. *et al.* Retina-Inspired Organic Photonic Synapses for Selective Detection of SWIR Light. *Angewandte Chemie International Edition* **62**, e202213733 (2023).

### **Acknowledgments**

This research is financially supported by the National Key R&D Program of China (2019YFA0705201), the National Basic Research Program of China (2019YFB1310200).

### **Author contributions**

P.-A. Hu supervised the project. Q. Wang conceived the ideas and designed the experiments. Q. Wang synthesized and measured the materials. Q. Wang and P.F. Li fabricated and measured the devices. G.L. Ma and Y.S. Song provided radiation sources. J.L. Li, H.Y. Xiao and Y.Q. Wang assisted in the experiment. P.-A. Hu, Q. Wang and H.-S Tsai analyzed the experimental data and co-wrote the paper. Q. Wang and P.F. Li contributed equally. H.-S Tsai and P.-A. Hu are co-corresponding. All the authors discussed the results and commented on the manuscript.

### **Competing interests**

The authors declare no competing interests.